
GWRF: A Generalizable Wireless Radiance Field for Wireless Signal Propagation Modeling

Kang Yang¹ Yuning Chen¹ Wan Du¹

Abstract

We present Generalizable Wireless Radiance Fields (*GWRF*), a framework for modeling wireless signal propagation at arbitrary 3D transmitter and receiver positions. Unlike previous methods that adapt vanilla Neural Radiance Fields (NeRF) from the optical to the wireless signal domain—requiring extensive per-scene training—*GWRF* generalizes effectively across scenes. First, a geometry-aware Transformer encoder-based wireless scene representation module incorporates information from geographically proximate transmitters to learn a generalizable wireless radiance field. Second, a neural-driven ray tracing algorithm operates on this field to automatically compute signal reception at the receiver. Experimental results demonstrate that *GWRF* outperforms existing methods on single scenes and achieves state-of-the-art performance on unseen scenes. The code will be publicly released.

1. Introduction

The evolution of wireless communication systems, such as WiFi and 5G cellular networks, has enabled transformative applications in areas like smart cities and precision agriculture (Gadre et al., 2020; Tong et al., 2023). These networks serve as both communication backbones and sensing platforms. Reliable communication requires meticulous network planning to address issues like dead spots and outages (Ahamed & Faruque, 2021), while sensing applications—such as WiFi-based localization (Ayyalasomayajula et al., 2020; Yang et al., 2024; Savvides et al., 2001)—depend on extensive, high-quality data for deep neural network (DNN) training. Traditionally, site surveys (Kar & Dappuri, 2018) are conducted to collect signal strength data for planning and sensing purposes, requiring dense measurements at various locations. However, these site surveys are time-intensive and costly (Cisco, 2023).

¹University of California, Merced, California, USA. Correspondence to: Wan Du <wdu3@ucmerced.edu>.

Wireless signal propagation modeling offers an efficient alternative by predicting the received signal at the receiver given the transmitter and receiver positions, while accounting for signal attenuation, phase rotation, and interference (Kouyoumjian & Pathak, 1974; Na & Eibert, 2022). For instance, in free space, Maxwell’s equations (Maxwell, 1873) can accurately calculate the received signal (Wong et al., 1984). However, obstacles in real-world environments make these equations unsolvable (Zhao & Chew, 2000). To address this, ray tracing simulations (Yun & Iskander, 2015; Egea-Lopez et al., 2021; MATLAB, 2023) attempt to model signal propagation paths using Computer-Aided Design (CAD) scene models. Nevertheless, the difficulty of obtaining accurate and realistic CAD models makes these simulations both impractical and unreliable.

Recently, NeRF² (Zhao et al., 2023) and NeWRF (Lu et al., 2024) have adapted vanilla Neural Radiance Fields (NeRF), originally designed for novel view synthesis in the optical domain (Tancik et al., 2022; Liu et al., 2020), to model wireless signal propagation. These methods achieve state-of-the-art accuracy in predicting received signals by learning neural radiance fields specific to wireless signals. However, like vanilla NeRF, they are prone to overfitting the scenes they are trained on, necessitating time-intensive training for each new scene (Wang et al., 2021; Liu et al., 2022).

This paper introduces *GWRF*, Generalizable Wireless Radiance Fields, which improves wireless signal propagation modeling in single scenes and enables generalization to unseen scenes. In the optical domain, generalizable neural radiance fields (Chen et al., 2021; Trevithick & Yang, 2021; Wang et al., 2021; Liu et al., 2022) have been developed based on view interpolation theory (Chen & Williams, 1993). These models generalize by interpolating images across camera views, capturing shared geometric and appearance features from multiple perspectives. In contrast, equivalent view interpolation theory for the wireless signal domain remains unexplored. To address this gap, we demonstrate that the spatial spectrum—representing received signal strength from all directions at the receiver (see Section 2.1)—for a transmitter can be interpreted as an interpolation of the spectra of its geographically proximate neighboring transmitters. By leveraging the spectra of these neighbors, *GWRF* learns

a generalizable wireless radiance field, enabling spatial spectrum inference in unseen scenes.

Constructing generalizable wireless radiance fields requires a fundamentally different approach from optical radiance fields due to their distinct propagation behaviors, driven by the nanometer-scale wavelengths of light compared to the centimeter-scale wavelengths of wireless signals. Visible light primarily reflects off surfaces (Pathak et al., 2015), enabling optical radiance field methods to compute voxel attributes, i.e., color and opacity, by integrating multi-view images (Chen et al., 2021; Trevithick & Yang, 2021). In contrast, wireless signals interact with obstacles in more complex ways, including absorption, reflection, diffraction, and scattering (Kouyoumjian & Pathak, 1974; Na & Eibert, 2022). This complexity makes two-attribute voxel representations insufficient for modeling wireless signal propagation. Such representations limit modeling precision within individual scenes and hinder generalization to unseen environments. To address these challenges, we propose representing voxel attributes as latent vectors within a latent voxel feature space. This space is constructed using a geometry-aware Transformer encoder with a cross-attention mechanism, which processes the spatial spectra of neighboring transmitters and their positional relationships with the target transmitter. By capturing the intricate propagation behaviors of wireless signals and geometry-dependent features, *GWRF* improves voxel representation and facilitates generalization.

Furthermore, since each voxel’s attributes are represented as a latent vector rather than two single values—such as signal emission and attenuation in NeRF² or color and opacity in optical radiance fields—we propose a novel neural-driven ray tracing algorithm to compute the received signal. This algorithm emits rays in all directions from the receiver, with each ray sampling multiple voxels along its path. The sampled voxels are interpreted as sequential tokens, and a Transformer architecture aggregates their features to compute the received signal. As voxel vectors may encode both amplitude and phase information inherent to wireless signals, the Transformer is designed as a multi-head model to capture diverse relationships among voxel features.

Extensive experimental results confirm that *GWRF* infers high-quality spatial spectra in both seen and unseen scenes. A case study on spectrum-based Angle of Arrival (AoA) estimation showcases *GWRF*’s effectiveness for downstream tasks. Our key contributions are summarized as follows:

- We present *GWRF*, the first generalizable wireless radiance field framework for modeling wireless signal propagation, capable of generalizing to unseen scenes.
- We identify that the spatial spectrum of a transmitter can be interpreted as an interpolation of spectra from its geographically proximate transmitters.

- We propose a geometry-aware scene representation module with a cross-attention layer to effectively fuse neighboring spatial spectra for learning voxel latent features.
- We develop a neural-driven ray tracing algorithm that incorporates complex-valued wireless signal characteristics to achieve accurate spatial spectrum synthesis.

In summary, we propose *GWRF*, a generalizable framework for wireless signal propagation modeling, enabling more flexible and efficient wireless communication and sensing applications across diverse environments. Details of the impact statements are summarized in Section 7.

2. Preliminary

In this section, we provide the background on spatial spectrum and vanilla NeRF for wireless signal modeling.

2.1. Spatial Spectrum

The spatial spectrum represents the received signal power distribution around the receiver for a signal transmitted by a transmitter. In this section, we describe the wireless channel and then outline the computation of the spatial spectrum.

2.1.1. WIRELESS CHANNEL

A wireless communication system consists of a transmitter and a receiver. The transmitted signal can be expressed as a complex number $x = Ae^{j\psi}$, where A represents the amplitude, and ψ denotes the phase. As the signal propagates through the wireless channel, its amplitude is attenuated by A_{att} , and its phase is shifted by $\Delta\psi$. The signal received at the receiver with a single antenna can be written as:

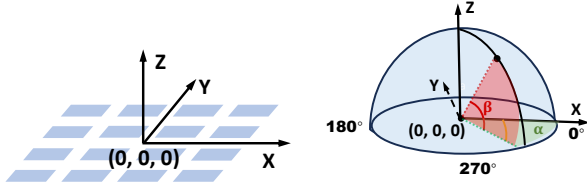
$$y = x \cdot A_{\text{att}}e^{j\Delta\psi} = A \cdot A_{\text{att}}e^{j(\psi+\Delta\psi)} \quad (1)$$

Antenna Array. For a receiver configured as an antenna array with $K \times K$ elements, as shown in Figure 1(a), the received signal is represented as a matrix $\mathbf{Y} = [y_{m,n}]_{m,n=0}^{K-1}$, where $y_{m,n}$ denotes the signal received at the (m, n) -th element of the array. Each element $y_{m,n}$ is given by:

$$y_{m,n} = A \cdot A_{\text{att}}e^{j(\psi+\Delta\psi+\Delta\sigma_{m,n})} \quad (2)$$

where $A_{\text{att}}e^{j\Delta\psi}$ represents the attenuation and phase shift introduced by the wireless channel. This is assumed to be uniform across all elements due to the small array aperture relative to the propagation distance (Van Trees, 2002). The term $\Delta\sigma_{m,n}$ is the geometric phase shift caused by the position of the (m, n) -th element relative to the array center at $(0, 0, 0)$. It is determined by the element’s position and the angles of arrival of the incoming signal:

$$\Delta\sigma_{m,n} = \frac{2\pi}{\lambda} (md \sin \beta \cos \alpha + nd \sin \beta \sin \alpha) \quad (3)$$



(a) Receiver: 4×4 antenna array (b) Azimuth α and elevation β
 Figure 1. Antenna array, each blue square as a single antenna.

where λ is the signal wavelength, $d = \frac{\lambda}{2}$ is the element spacing, and α and β are the azimuth and elevation angles of the incoming signal, respectively, as shown in Figure 1(b).

2.1.2. COMPUTING SPATIAL SPECTRUM

The spatial spectrum is computed from the received signal matrix \mathbf{Y} to estimate power distribution over azimuth α and elevation β . For a given direction (α, β) , the power is:

$$\mathbf{SS}(\alpha, \beta) = \left| \sum_{m=0}^{K-1} \sum_{n=0}^{K-1} y_{m,n} e^{-j\Delta\sigma_{m,n}} \right|^2 \quad (4)$$

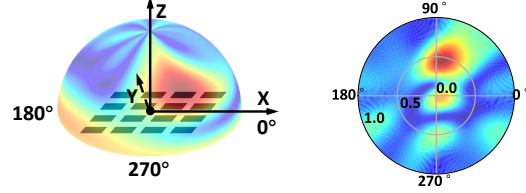
where $\Delta\sigma_{m,n}$ is the theoretical geometric phase shift from Equation (3). With one-degree resolution and only the upper hemisphere considered, the spatial spectrum \mathbf{SS} is a matrix of dimensions $(360, 90)$: $\mathbf{SS} = [S_{p,q}]_{p,q=0}^{359,89}$. Figure 2(a) illustrates the 3D spatial spectrum with one-degree directional resolution. Figure 2(b) then depicts the 2D spectrum, which is the 3D view projected onto the X-Y plane, with the radial distance representing $\cos(\beta)$.

2.2. Vanilla NeRF for Wireless Signal Modeling

Vanilla NeRF has recently been adapted for wireless signal modeling (Zhao et al., 2023; Lu et al., 2024). It models a scene using an MLP with 8-dimensional inputs:

$$\mathcal{F}_{\Theta} : (\{x, y, z\}, \alpha, \beta, \{x_{tx}, y_{tx}, z_{tx}\}) \rightarrow (\delta, \xi) \quad (5)$$

where $\{x, y, z\}$ are the 3D spatial coordinates of a voxel, and (α, β) are the azimuth and elevation angles defining the 2D view direction of a ray traced from the receiver. The transmitter’s 3D coordinates $\{x_{tx}, y_{tx}, z_{tx}\}$ are also considered, as each voxel’s properties in the wireless domain are influenced by the signal source location. The outputs (δ, ξ) represent wireless signal properties of the voxel, where δ is the attenuation and ξ is the signal emission, with each voxel treated as a new wireless signal source according to the Huygens–Fresnel principle (Born & Wolf, 2013). To generate the spatial spectrum, NeRF² (Zhao et al., 2023) performs ray tracing in each direction of the spectrum. Discrete sample voxels $\{V_1, \dots, V_S\}$ are taken along each ray \mathbf{r} , and the MLP is queried with their coordinates to predict δ



(a) 3D view (b) 2D projection view

Figure 2. Illustration of 3D and 2D views of the spatial spectrum.

and ϵ . The result for each ray $\mathbf{SS}(\mathbf{r})$ is calculated as:

$$\mathbf{SS}(\mathbf{r}) = \sum_{i=1}^S \exp \left(\sum_{j=1}^{i-1} \delta_j \right) \xi_i \quad (6)$$

This equation calculates the aggregation of signals retransmitted by voxels along the ray, where each voxel acts as a new source, and transmissions are attenuated by intervening voxels between the source and the receiver.

3. Related Work

Generalization on Optical NeRF. Optical NeRF has revolutionized novel view synthesis by learning 3D scene representations from 2D images. However, traditional NeRF requires extensive per-scene training, limiting its generalization to new scenes. Generalizable NeRF approaches overcome this limitation by adapting to unseen scenes without retraining (Trevithick & Yang, 2021; Chen et al., 2021; Xu et al., 2023; Chou et al., 2024; Tian et al., 2023; Liu et al., 2022). For example, MVSNerf integrates multi-view stereo with neural rendering to reconstruct radiance fields from a few input views (Chen et al., 2021), and WaveNeRF employs wavelet-based representations for generalization (Xu et al., 2023). GSNeRF incorporates semantics to generate novel views and semantic maps for unseen scenes (Chou et al., 2024), while NeuRay aggregates image features from multiple views to predict voxel properties (Liu et al., 2022). These methods, designed for visible light, cannot be directly applied to wireless signals due to fundamental differences in wavelength and propagation behaviors. This work extends generalizable NeRF to the wireless domain for spatial wireless signal propagation modeling.

NeRF for Wireless Signal Modeling. There are pioneering efforts that have explored NeRF for wireless signal modeling (Zhao et al., 2023; Orekondy et al., 2023). For instance, NeRF² trains an MLP to compute voxel attributes and proposes Equation (6) as the ray tracing algorithm to compute the received signal for each ray. However, it requires scene-specific training, which limits scalability and generalization to new environments. NeWRF (Lu et al., 2024) leverages direction-of-arrivals (DoA) as priors to reduce the required rays, thereby enhancing the efficiency of signal reception

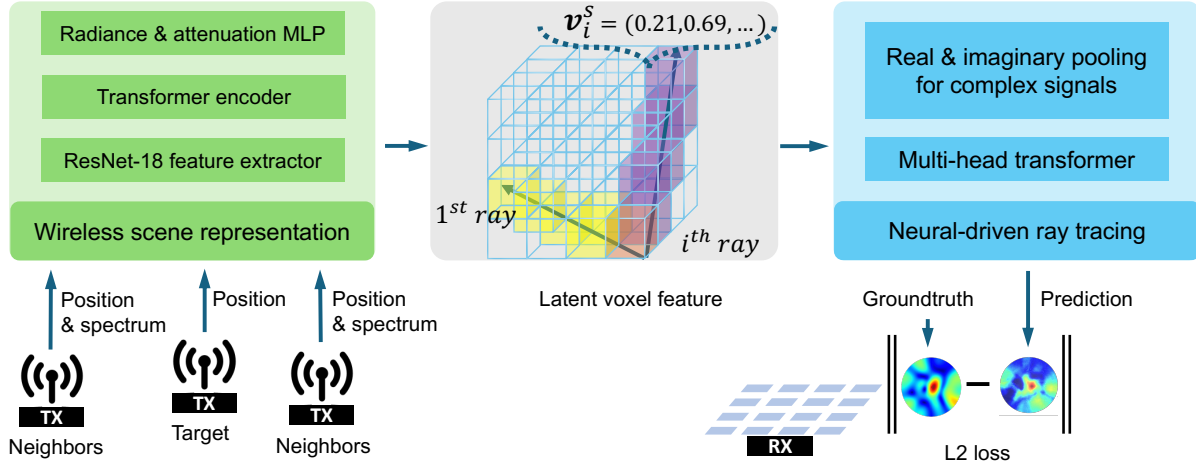


Figure 3. Architecture of *GWRF*. Each voxel is represented by a feature \mathbf{v}_i^s , where i indexes the M rays, and s denotes the voxel’s position along the i -th ray. A neural-driven ray tracing algorithm computes the received signal power for each ray (TX: transmitter, RX: receiver).

computation. However, this efficiency comes at the cost of requiring additional antenna arrays for DoA data collection, which are infeasible in complex, obstructed environments. *GWRF* avoids this additional data requirement. *WiNeRT* (Orekondy et al., 2023) employs differentiable ray tracing with scene CAD models, which is impractical due to the difficulty of obtaining accurate CAD models. In contrast, *GWRF* eliminates this dependency, offering a more practical and flexible solution. More importantly, these models lack generalization. *GWRF* introduces generalizable neural radiance fields for wireless signal propagation, adapting to unseen scenes without scene-specific training.

4. GWRF

4.1. Task Objective

We consider a real-world scenario where receivers (e.g., 5G base stations) are fixed with antenna arrays, while transmitters (e.g., smartphones) are randomly placed throughout the scene. At each transmitter position, the transmitter emits wireless signals, and the receiver measures the spatial spectrum. In *GWRF*, rays are emitted from the receiver in each direction of the spatial spectrum. These rays interact with objects through reflection, diffraction, and scattering (Bonde-son et al., 2012). These rays interact with objects, experiencing reflection, diffraction, scattering, and so on (Bonde-son et al., 2012). For a spatial spectrum \mathbf{SS} of dimensions $(360, 90)$, $M = 360 * 90$ rays are emitted, each computing signal power for its respective direction. The objective is to predict the spatial spectrum at the receiver for any transmitter location in the scene.

4.2. Overview

As illustrated in Figure 3, *GWRF* synthesizes the spatial spectrum at the receiver, given the L neighboring transmitters’ spatial spectra with their positions $\{\mathbf{SS}_i \in \mathbb{R}^{360 \times 90}, \mathbf{P}_i \in \mathbb{R}^{3 \times 1}\}_{i=1}^L$, and the target transmitter position $\{x_{tx}, y_{tx}, z_{tx}\}$. It constructs a wireless scene representation in a latent voxel space as:

$$\mathbf{v} = \mathcal{F}_\Theta(\{(\mathbf{SS}_1, \mathbf{P}_1), \dots, (\mathbf{SS}_L, \mathbf{P}_L)\}, \{x, y, z\}, \alpha, \beta, \{x_{tx}, y_{tx}, z_{tx}\}) \quad (7)$$

where the network \mathcal{F}_Θ is a general wireless radiance field (*GWRF*) that parameterizes scenes observed from the input L spectra and returns the voxel feature when queried at any location $\{x, y, z\}$. Next, voxel features are traced along rays using the proposed neural-driven ray tracing algorithm to generate the spectrum for the target transmitter position. Preliminary experiments, detailed in Appendix A, illustrate why neighboring spatial spectra are beneficial.

4.3. Wireless Scene Representation

Instead of outputting variables such as the attenuation δ and signal emission ξ , as defined in Equation (5), in this module, each voxel’s attribute is represented as a latent feature \mathbf{v} . It consists of ResNet-18 feature extractor (He et al., 2016), geometry-aware Transformer encoder with cross-attention mechanism (Gheini et al., 2021), and two MLP networks.

ResNet-18 Spatial Spectrum Feature Extractor. Directly inputting the raw spatial spectra into the Transformer encoder is memory-prohibitive, as it requires calculating attention scores for all spectrum pairs. To address this, we use a ResNet-18 encoder to extract compact spectrum features $\{\mathbf{f}_l\}_{l=1}^L$, where each \mathbf{f}_l serves as a token for the Transformer encoder. These spectrum features are organized into a matrix for the Transformer, with each column representing an

extracted spectrum feature. The resulting matrix has dimensions (d, L) , where d is the feature dimension of each token, and L is the number of tokens:

$$\mathbf{F} = [\mathbf{f}_1 \quad \mathbf{f}_2 \quad \cdots \quad \mathbf{f}_L], \quad \mathbf{F} \in \mathbb{R}^{d \times L} \quad (8)$$

Transformer Encoder. The attention mechanism (Gheini et al., 2021) captures the influence of positional variations on the spatial spectrum. To model these positional differences, we subtract the Key matrix \mathbf{K} from the Query matrix \mathbf{Q} , process the result with an MLP, and apply the softmax function to compute attention scores. These scores weight the Value matrix \mathbf{V} , which incorporates positional differences via position encoding \mathcal{E} . The position encoding converts 3D positions into high-dimensional vectors to model positional relationships. The process is formally expressed as:

$$\gamma = \text{softmax}(\mathcal{MLP}(\mathbf{K} - \mathbf{Q})) \cdot (\mathbf{V} + \mathcal{E}(\mathbf{P}_{\text{neighbor}} - \mathbf{P}_{\text{target}})), \quad (9)$$

$$\mathbf{Q} = \mathbf{W}_Q \cdot \mathbf{F}, \quad \mathbf{K} = \mathbf{W}_K \cdot \mathbf{F}, \quad \mathbf{V} = \mathbf{W}_V \cdot \mathbf{F}$$

where \mathbf{W}_Q , \mathbf{W}_K , and \mathbf{W}_V are learnable matrices, and $\mathbf{P}_{\text{neighbor}}$ and $\mathbf{P}_{\text{target}} = \{x_{tx}, y_{tx}, z_{tx}\}$ are the 3D positions of the neighbors and target transmitter, respectively. This representation γ encapsulates the geometric relationships between positions and their corresponding spatial spectra.

MLP Networks. The learned representation γ is shared across all voxels associated with the target transmitter and its neighbors. To compute voxel-specific features, γ is combined with the voxel position $\{x, y, z\}$ and passed through two MLP networks. The attenuation MLP $\mathcal{MLP}_{\text{att}}$ models the position-dependent attenuation feature for the voxel. The radiance MLP $\mathcal{MLP}_{\text{rad}}$, which learns the voxel's emitted signal feature, takes additional inputs: the target transmitter position $\{x_{tx}, y_{tx}, z_{tx}\}$ and the voxel's direction relative to the receiver (α, β) , capturing dependencies on both the source signal and directional information. Finally, the outputs of the two MLPs are concatenated to form the latent voxel feature $\mathbf{v} \in \mathbb{R}^d$. This process is expressed as:

$$\mathbf{v} = \mathcal{MLP}_{\text{att}}(\gamma, \{x, y, z\}) \oplus \mathcal{MLP}_{\text{rad}}(\gamma, \{x, y, z\}, \alpha, \beta, \{x_{tx}, y_{tx}, z_{tx}\}) \quad (10)$$

4.4. Neural-Driven Ray Tracing Algorithm

The simplified aggregation process defined in Equation (6) can be interpreted as a weighted sum of voxel-wise emitted signals, where the weights are determined by the attenuation from other voxels along the ray. This process can be effectively modeled using a Transformer architecture by mapping voxel-wise features (δ, ξ) into token features, with attention scores representing the cumulative attenuation.

Figure 4 illustrates the proposed neural-driven ray tracing algorithm. It utilizes a standard transformer encoder architecture, but here we focus on the core attention mechanism.

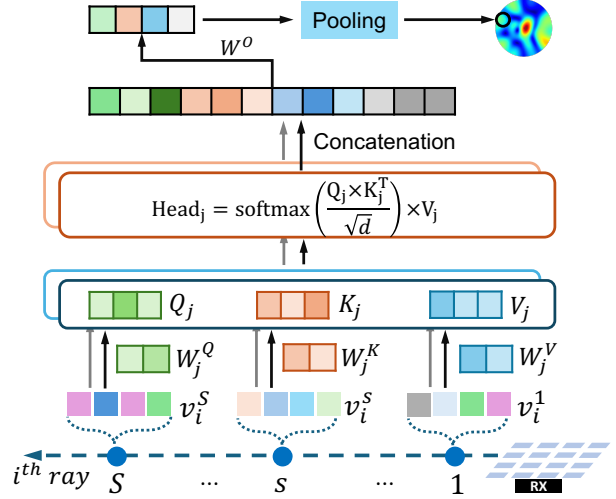


Figure 4. Architecture of the neural-driven ray tracing algorithm, where S voxels are sampled along the i -th ray (RX: receiver).

Along the ray, S voxels are sampled, and their latent features $\{\mathbf{v}^s\}_{s=1, \dots, S}$ are extracted, with each \mathbf{v}^s treated as a token. The attention scores are computed using the softmax function applied to the scaled product of the Query matrix \mathbf{Q} and Key matrix \mathbf{K} , where d is the voxel feature dimension. The scores weight the Value matrix \mathbf{V} , resulting in an aggregated latent voxel feature across all S voxels:

$$\text{Attention}(\mathbf{Q}, \mathbf{K}, \mathbf{V}) = \text{softmax}\left(\frac{\mathbf{Q}\mathbf{K}^T}{\sqrt{d}}\right) \mathbf{V} \quad (11)$$

Each voxel feature implicitly encodes the real and imaginary parts of the signal and attenuation, allowing attention scores to capture their complex relationships. Among these, all possible pairwise combinations total $\binom{4+2-1}{2} = 10$, leading to the use of ten attention heads in the transformer to effectively model these dynamics. Each head is equipped with distinct learnable projection matrices \mathbf{W}_Q^j , \mathbf{W}_K^j , and \mathbf{W}_V^j , where j indexes the head from 1 to 10. The output of each head, Head_j , is concatenated into a new feature, which is then multiplied by another learnable projection matrix \mathbf{W}_o to produce the predicted feature for each voxel along the current i -th ray. Finally, mean pooling is performed over all voxels along the ray, and the pooled feature vector is mapped to the real and imaginary parts of the received signal. The amplitude of the resulting signal is calculated as the predicted signal power for the ray.

4.5. Implementation Details

Training. *GWRP* is trained end-to-end using the L2 loss function, computed per ray as the ray tracing algorithm processes each ray individually, to minimize the difference between the predicted and ground truth signal power. Training is optimized with the Adam optimizer (Kingma & Ba,

2015), starting with an initial learning rate of 5.0×10^{-4} , which decays exponentially. *GWRF* is trained for 300,000 steps over approximately 15 hours, with 5,120 rays sampled from the spatial spectrum at each step. Further details on the network architecture are provided in Appendix B.

Neighbors Selection Strategy. A target transmitter is paired with its geographically closest transmitters, selecting L neighbors based on Euclidean distance. To account for varying neighbor densities, L is randomly chosen within the range $[3, 10]$ for each target transmitter. This strategy ensures adaptability to diverse spatial distributions of transmitters. During testing, L neighbors are chosen from the training split of the testing scene’s data.

Positional encoding \mathcal{E} . For the 3D coordinates of transmitter positions, neighbors’ positions, and ray positions and directions, we transform these low-dimensional coordinates into high-dimensional representations using the Position Embedding function (Vaswani et al., 2017), with 10 frequency bands in all experiments. This expands the 3D coordinates from 3 to $3 + 3 \times 10 \times 2 = 63$ dimensions. In cross-scene experiments, where each transmitter position includes 3D coordinates and a scene index, the 4D coordinates are expanded to $4 + 4 \times 10 \times 2 = 84$ dimensions. This transformation allows the network to distinguish identical coordinates across different scenes.

5. Experiments

We first evaluate *GWRF* in a single-scene setting, followed by a cross-scene generalization setting.

5.1. Experimental Protocols

5.1.1. DATASETS

RFID Dataset. Introduced by NeRF² (Zhao et al., 2023), the Radio-Frequency Identification (RFID) wireless system operates in the 915 MHz frequency band, with a receiver positioned at a fixed location and equipped with a 4×4 antenna array. The dataset consists of 6,123 transmitter locations, each associated with a spatial spectrum.

MATLAB Dataset. We consider two representative layouts: a conference room and an office room. Their geometries are illustrated in Figure 5, with dimensions of $9.8ft \times 9.8ft \times 8.2ft$ and $26.2ft \times 16.4ft \times 9.8ft$, respectively. Each layout is represented by a CAD model, modified in Blender (Blender, 2024) to add or remove objects. In Figure 5(a), for the conference room layout, three scene versions are created by varying chair placements: with chairs 1 and 2 (**ConferenceV1**), with only chair 1 (**ConferenceV2**), and with neither chair 1 nor chair 2 (**ConferenceV3**). Similarly, in Figure 5(b), for the office room layout, three scene versions are created by varying table placements: with both

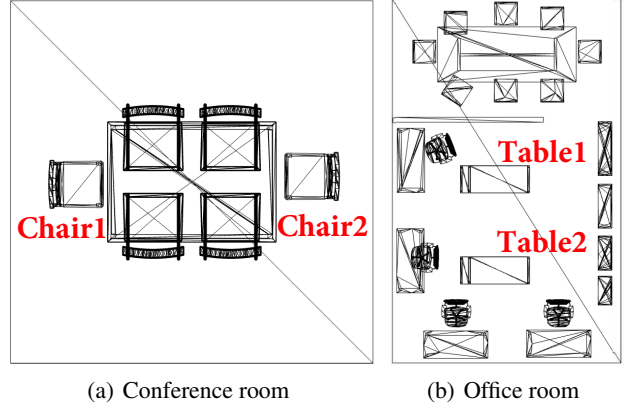


Figure 5. Top-view visualization of two representative layouts.

tables 1 and 2 (**OfficeV1**), with only table 1 (**OfficeV2**), and with neither table 1 nor table 2 (**OfficeV3**).

In each scene version, a receiver with a fixed antenna array is positioned, and transmitters are randomly distributed throughout the space. A total of 4,416, 4,453, 3,107, 8,481, 7,274, and 4,894 transmitters are placed to collect spatial spectra for each scene version using MATLAB ray tracing simulation (MATLAB, 2023). Unless stated otherwise, 80% of the data is for training and 20% for testing.

5.1.2. BASELINES

We compare *GWRF* against three baseline methods.

i) K-Nearest Neighbors (KNN): Predicts the spatial spectrum at a target transmitter location by averaging the spectra of the L nearest neighbors from the training set, ensuring L matches *GWRF* for a fair comparison.

ii) KNN-DL: Similar to the KNN method, this approach assigns a weight matrix of dimension $(360, 90)$ to each neighbor instead of equally averaging. Each pixel of the spectrum is assigned a specific weight, and the target transmitter’s spectrum is predicted through a weighted summation of all neighbors’ spectra using their learned weight matrices. The weight matrices are optimized with the L2 loss function. Further details are provided in Appendix A.

iii) NeRF² (Zhao et al., 2023): The method is introduced in Section 2.2. NeWRF (Lu et al., 2024) is essentially identical to NeRF², except it uses additional DoA data to reduce the number of rays. Since DoA data is difficult to obtain, we treat NeRF² and NeWRF as equivalent methods.

5.1.3. METRICS

Signal power prediction is evaluated as a regression task with Mean Squared Error (MSE). Since the spatial spectrum, visualized in Figure 2(b), resembles an image, image quality metrics assess pixel-level differences and struc-

Table 1. Comparison of *GWRF* against baseline methods for single-scene setting. Results are averaged across all 7 scenes.

Models	MSE↓	LPIPS↓	PSNR↑	SSIM↑
KNN	0.089	0.357	15.16	0.543
KNN-DL	0.048	0.198	20.81	0.675
NeRF ²	0.052	0.274	19.93	0.704
<i>GWRF</i>	0.038	0.136	21.94	0.766

tural information (Wang et al., 2004), capturing directional patterns. Therefore, the evaluation involves four widely adopted metrics: MSE↓, Learned Perceptual Image Patch Similarity (LPIPS↓), Peak Signal-to-Noise Ratio (PSNR↑), and Structural Similarity Index Measure (SSIM↑).

5.2. Single-Scene Performance

There are 7 scenes in total: 1 from the RFID dataset and 6 from the MATLAB dataset (ConferenceV1, ConferenceV2, ConferenceV3, OfficeV1, OfficeV2, and OfficeV3). In this section, we train and test a single model for each scene, using 80% of the data samples for training and the remaining 20% for testing. Table 1 presents the average quantitative results across all 7 scenes.

Analysis. We first present the spatial spectra of four randomly selected transmitter locations, alongside the spectra synthesized by NeRF² and *GWRF*, as illustrated in Figure 6. Visually, the spectra synthesized by *GWRF* closely match the ground truth, outperforming those generated by NeRF². Consistent with this visual comparison, *GWRF* achieves superior metric scores, as illustrated in Table 1. Compared to the KNN and KNN-DL methods, *GWRF* improves PSNR by 44.7% and 5.5%, respectively. These results demonstrate that neighboring spatial spectra are indeed helpful for predicting the target transmitter’s spectrum. However, KNN’s simple averaging approach fails to capture the intricate spatial relationships among the neighboring spectra. KNN-DL further improves upon KNN’s performance, indicating that a careful interpretation of neighboring spectra can enhance the prediction accuracy. Nevertheless, KNN-DL does not account for the geometric relationships among spectra, limiting its effectiveness. Finally, *GWRF* outperforms NeRF² by 26.9%, 50.4%, 10.2%, and 8.8% in terms of MSE, LPIPS, PSNR, and SSIM, respectively. This improvement highlights *GWRF*’s ability to leverage neighboring spatial spectra to learn latent voxel features that capture complex propagation behaviors and dynamically assign weights using an attention mechanism during ray tracing.

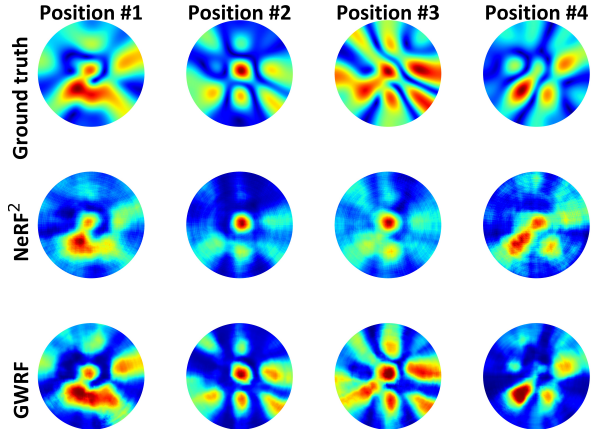


Figure 6. Visual comparison of spatial spectra generated by NeRF² and *GWRF* at four randomly selected transmitter positions.

5.3. Generalization to Unseen Scenes

We then assess our method’s generalization across unseen scenes. Specifically, we evaluate how *GWRF* performs when the scene’s objects are altered. In this study, we train two separate models for the conference room and office room layouts. For the conference layout model, training is conducted on ConferenceV1, with testing performed on the test splits of ConferenceV2 and ConferenceV3. Similarly, for the office layout model, training is conducted on OfficeV1, and testing is performed on the test splits of OfficeV2 and OfficeV3. The three baseline methods are trained and tested under identical settings for comparison.

Analysis. Table 2 presents the average quantitative results for the two layout models. When compared to the single-scene setting (Table 1), KNN demonstrates similar performance across both settings, emphasizing that neighboring spatial information remains consistently beneficial. In contrast, the performance of KNN-DL and NeRF² declines in the unseen scene setting due to their reliance on models specifically tailored to the training scenes, limiting their generalization capabilities. However, since the differences between the tested and trained scenes involve only minor variations, such as the addition or removal of one or two tables or chairs, the performance degradation for KNN-DL and NeRF² is moderate, with PSNR drops of 8.51% and 12.90%, respectively. In comparison, *GWRF* achieves the highest accuracy in both settings by leveraging geometry-aware voxel features and a neural-driven ray tracing algorithm, enabling generalization across diverse scenes.

5.4. Generalization to Unseen Layouts

We further evaluate the generalization of *GWRF* under a more challenging setting. Specifically, a model is trained on the three scene versions of the conference layout, i.e., the training splits of ConferenceV1, ConferenceV2, and

Table 2. Comparison of *GWRF* with baselines on unseen scenes.

Models	MSE↓	LPIPS↓	PSNR↑	SSIM↑
KNN	0.083	0.361	14.77	0.552
KNN-DL	0.053	0.279	19.04	0.614
NeRF ²	0.065	0.337	17.36	0.691
<i>GWRF</i>	0.039	0.215	20.96	0.705

Table 3. Comparison of *GWRF* with baselines on unseen layouts.

Models	MSE↓	LPIPS↓	PSNR↑	SSIM↑
KNN	0.085	0.359	15.32	0.539
KNN-DL	0.087	0.429	14.94	0.498
NeRF ²	0.092	0.477	12.76	0.481
<i>GWRF</i>	0.042	0.268	17.81	0.629

ConferenceV3, and tested on the three scenes of the office layout, i.e., OfficeV1, OfficeV2, and OfficeV3. The reverse experiment is also conducted, where the model is trained on OfficeV1, OfficeV2, and OfficeV3, and tested on ConferenceV1, ConferenceV2, and ConferenceV3.

Analysis. Table 3 presents the quantitative results for unseen layouts. KNN demonstrates consistent performance across settings with slight PSNR fluctuations, reflecting the effectiveness of neighboring spatial spectrum information. In contrast, KNN-DL and NeRF² show significant performance declines in unseen layouts compared to single-scene settings. KNN-DL’s PSNR drops by 28.2% and NeRF²’s by 35.9%, highlighting their limited generalization due to scene-specific training. *GWRF* achieves the highest accuracy across all settings, demonstrating robust generalization. This is attributed to its geometry-aware voxel features and neural-driven ray tracing algorithm, which enable it to adapt to diverse environments. However, the spectra synthesized by *GWRF* in cross-layout experiments are of lower quality than those in single-scene experiments. This decline is due to challenges posed by varied layouts and object materials (Wong et al., 1984). Fine-tuning *GWRF* with data from new scenes could further improve spectrum quality.

5.5. Ablation Study

To evaluate the key components of *GWRF*, we conduct experiments based on the unseen scene settings in Section 5.3.

Wireless Scene Representation. We replace the cross-attention layer with a dot-product attention layer to learn wireless radiance fields. A comparison between the first and third rows in Table 4 indicates that *GWRF* achieves slightly better scores with the cross-attention mechanism. This result demonstrates that *GWRF*’s generalization relies less on the specific attention type and more on enabling interactions across neighboring spatial spectra.

Table 4. Average scores of PSNR and LPIPS for ablated *GWRF*.

Variations	LPIPS↓	PSNR↑
Remove cross-attention layer	0.239	19.37
Remove neural ray tracing	0.379	16.79
Full model (<i>GWRF</i>)	0.215	20.96

Neural-Driven Ray Tracing Algorithm. We replace our neural-driven ray tracing algorithm with the simplified tracing method defined in Equation (6). This modification adjusts the scene representation to output only two variables: signal emission and attenuation. A comparison between the second and third rows in Table 4 indicates that our neural-driven algorithm significantly outperforms the simplified method, emphasizing the benefits of voxel vector representation over simple attributes and its ability to automatically learn weights for effective fusion.

5.6. Impact of Wireless Signal Frequency Bands

To examine the impact of frequency bands on *GWRF*’s performance, we separately collect three datasets in a conference room (Figure 5(a)) at 928 MHz, 2.412 GHz, and 5.805 GHz. *GWRF* is trained separately on each dataset. Table 5 illustrates that *GWRF* adapts well to different frequency bands while maintaining high-quality spectra. Separate models are reasonable as each band supports distinct wireless technologies, such as 5G and WiFi, requiring dedicated hardware for signal reception and processing.

5.7. Case Study: Angle of Arrival (AoA) Estimation

The synthesized spectrum is valuable for downstream tasks such as Angle of Arrival (AoA) estimation (An et al., 2020). An angular artificial neural network (AANN) consists of a ResNet-50 backbone and an MLP head. It processes the spectrum to estimate the AoA, identifying the line-of-sight (LoS) propagation path direction between the transmitter and receiver. This LoS direction enables the localization of the transmitter’s position. By generating synthetic training datasets, *GWRF* significantly reduces the data collection effort required to train AANN. To highlight the advantages of the high-quality spectra synthesized by *GWRF*, we evaluate with the following two strategies:

1) Synthesized Spectra for AANN Training. An AANN is trained separately on four datasets: 50% ground truth (GT), 50% GT combined with 50% NeRF²-synthesized spectra, 50% GT combined with 50% *GWRF*-synthesized spectra, and 100% GT. All training datasets correspond to the same transmitter locations, and each trained AANN is tested on consistent testing transmitter locations. Figure 7(a) shows that the *GWRF*-augmented dataset reduces AoA estimation error by 61.6% compared to 50% GT alone and 25.8%

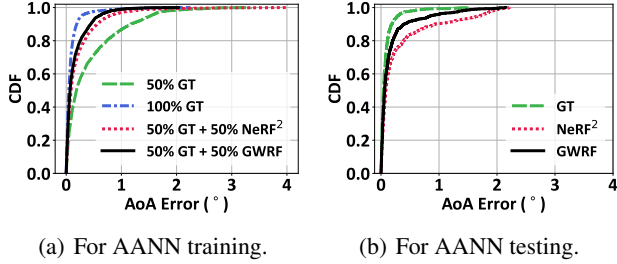


Figure 7. Spectrum-based AoA estimation using the AANN model.

compared to the NeRF²-augmented dataset. These results demonstrate that *GWRF* generates high-quality spectra that enhance localization-specific neural network training.

2) Synthesized Spectra for AANN Testing. An AANN is trained on GT spectra and evaluated on three types of test datasets: GT, NeRF²-synthesized spectra, and *GWRF*-synthesized spectra. All test spectra correspond to the same transmitter locations. Figure 7(b) demonstrates that *GWRF*'s spectra yield more accurate AoA estimations, highlighting the superior fidelity of *GWRF*'s synthesized spectra.

6. Conclusion

This paper presents *GWRF*, a generalizable wireless radiance field framework for modeling wireless signal propagation. *GWRF* integrates a geometry-aware scene representation module to capture geometrically related voxel features. It then incorporates a neural-driven ray tracing algorithm to aggregate features for signal power computation. Extensive experiments validate the generalization of *GWRF*.

7. Impact Statement

The proposed framework, *GWRF*, introduces a novel generalizable wireless radiance field for modeling wireless signal propagation, offering contributions to both machine learning research and practical applications in wireless communication and sensing. Below, we outline the broader scientific and societal impacts of this work:

1) Advancing ML for Wireless Domains. *GWRF* bridges the gap between optical and wireless domains by extending NeRF to wireless signal propagation modeling. Addressing the generalization challenges in unseen scenes, it contributes to the broader field of machine learning through advancements in spatial interpolation and geometry-aware learning tailored for non-optical domains. This work highlights the versatility of neural frameworks in tackling domain-specific challenges beyond their original applications.

2) Transforming Wireless Network Planning. Current approaches to network planning rely on expensive and time-intensive site surveys or Computer-Aided Design (CAD)-

Table 5. Effect of wireless signal frequency bands on performance.

	928 MHz	2.412 GHz	5.805 GHz
PSNR \uparrow	25.70	24.53	24.91

based simulations, which are often impractical in real-world environments. *GWRF* provides a scalable, data-driven alternative that improves the accuracy of signal propagation modeling while reducing the need for extensive manual data collection. This transformation has the potential to accelerate the deployment and optimization of wireless networks, including 5G and future communication technologies.

3) Improving Wireless Sensing Applications. Wireless sensing technologies, such as WiFi-based localization, rely on high-quality wireless signal data. By enabling generalizable spatial spectrum synthesis, *GWRF* provides high-quality data to train DNN models, improving the reliability and accuracy of these applications. Furthermore, *GWRF* can be utilized for quick evaluation of DNN models by providing accurate and generalizable signal data, reducing the need for extensive real-world data collection during the model development phase.

4) Supporting Equity in Wireless Access. By reducing the barriers to efficient network planning and sensing, *GWRF* has the potential to improve wireless coverage and sensing capabilities in underserved and remote areas.

In summary, *GWRF* represents a significant step toward integrating machine learning innovations into the wireless domain, with far-reaching implications for technology, research, and society. It lays the groundwork for more flexible, efficient, and cost-effective wireless communication systems that can adapt to diverse and dynamic environments.

This work does not raise any ethical issues.

Acknowledgments

Wan Du was partially supported by NSF Grant # 2239458, a UC Merced Fall 2023 Climate Action Seed Competition grant, and a UC Merced Spring 2023 Climate Action Seed Competition grant. Kang Yang was partially supported at UC Merced by a financial assistance award approved by the Economic Development Administration's Farms Food Future program.

References

Ahamed, M. M. and Faruque, S. 5G network coverage planning and analysis of the deployment challenges. *Sensors*, 21(19):6608, 2021.

An, Z., Lin, Q., Li, P., and Yang, L. General-Purpose Deep

- Tracking Platform across Protocols for the Internet of Things. In *Proceedings of the 18th ACM International Conference on Mobile Systems, Applications, and Services (MobiSys)*, 2020.
- Ayyalasomayajula, R., Arun, A., Wu, C., Sharma, S., Sethi, A. R., Vasisht, D., and Bharadia, D. Deep learning based wireless localization for indoor navigation. In *Proceedings of the 26th ACM Annual International Conference on Mobile Computing and Networking (MobiCom)*, 2020.
- Blender. Blender 4.2 LTS. <https://www.blender.org/>, 2024. [Online].
- Bondeson, A., Rylander, T., and Ingelström, P. *Computational electromagnetics*. Springer, 2012.
- Born, M. and Wolf, E. *Principles of Optics*. Cambridge University Press, 2013.
- Chen, A., Xu, Z., Zhao, F., Zhang, X., Xiang, F., Yu, J., and Su, H. MVSNerF: Fast Generalizable Radiance Field Reconstruction from Multi-View Stereo. In *IEEE/CVF International Conference on Computer Vision (ICCV)*, 2021.
- Chen, S. E. and Williams, L. View Interpolation for Image Synthesis. In *Proceedings of the ACM Special Interest Group on Computer Graphics and Interactive Techniques Conference (SIGGRAPH)*, 1993.
- Chou, Z.-T., Huang, S.-Y., Liu, I., Wang, Y.-C. F., et al. GSNeRF: Generalizable Semantic Neural Radiance Fields with Enhanced 3D Scene Understanding. In *IEEE/CVF Conference on Computer Vision and Pattern Recognition (CVPR)*, 2024.
- Cisco. Understand Site Survey Guidelines for WLAN Deployment. <https://www.cisco.com/c/en/us/support/docs/wireless/5500-series-wireless-controllers/116057-site-survey-guidelines-wlan-00.html>, 2023. [Online].
- Egea-Lopez, E., Molina-Garcia-Pardo, J. M., Lienard, M., and Degauque, P. Opal: An open source ray-tracing propagation simulator for electromagnetic characterization. *Plos one*, 16(11):e0260060, 2021.
- Gadre, A., Narayanan, R., Luong, A., Rowe, A., Iannucci, B., and Kumar, S. Frequency Configuration for Low-Power Wide-Area Networks in a Heartbeat. In *Proceedings of the 17th USENIX Symposium on Networked Systems Design and Implementation (NSDI)*, 2020.
- Gheini, M., Ren, X., and May, J. Cross-attention is all you need: Adapting pretrained transformers for machine translation. *arXiv preprint arXiv:2104.08771*, 2021.
- He, K., Zhang, X., Ren, S., and Sun, J. Deep residual learning for image recognition. In *IEEE/CVF Conference on Computer Vision and Pattern Recognition (CVPR)*, 2016.
- Kar, P. and Dappuri, B. Site Survey and Radio Frequency Planning for the Deployment of Next Generation WLAN. In *2018 International Conference on Wireless Communications, Signal Processing and Networking (WiSPNET)*, 2018.
- Kingma, D. P. and Ba, J. Adam: A method for stochastic optimization. In *International Conference on Learning Representations (ICLR)*, 2015.
- Kouyoumjian, R. and Pathak, P. A uniform geometrical theory of diffraction for an edge in a perfectly conducting surface. *Proceedings of the IEEE*, 62(11):1448–1461, 1974.
- Liu, L., Gu, J., Zaw Lin, K., Chua, T.-S., and Theobalt, C. Neural sparse voxel fields. *Advances in Neural Information Processing Systems*, 33:15651–15663, 2020.
- Liu, Y., Peng, S., Liu, L., Wang, Q., Wang, P., Theobalt, C., Zhou, X., and Wang, W. Neural Rays for Occlusion-aware Image-based Rendering. In *IEEE/CVF Conference on Computer Vision and Pattern Recognition (CVPR)*, 2022.
- Lu, H., Vatheuer, C., Mirzasoleiman, B., and Abari, O. NeWRF: A Deep Learning Framework for Wireless Radiation Field Reconstruction and Channel Prediction. In *Proceedings of the 41st ACM International Conference on Machine Learning (ICML)*, 2024.
- MATLAB. Indoor MIMO-OFDM Communication Link Using Ray Tracing. <https://www.mathworks.com/help/comm/ug/indoor-mimo-ofdm-communication-link\protect\penalty\z@-using-ray-tracing.html>, 2023. [Online].
- Maxwell, J. C. *A Treatise on Electricity and Magnetism*, volume 1. Oxford: Clarendon Press, 1873.
- Na, H. and Eibert, T. F. A Huygens’ Principle Based Ray Tracing Method for Diffraction Calculation. In *Proceedings of the the 16th IEEE European Conference on Antennas and Propagation (EuCAP)*, 2022.
- Orekondy, T., Kumar, P., Kadambi, S., Ye, H., Soriaga, J., and Behboodi, A. WiNeRT: Towards Neural Ray Tracing for Wireless Channel Modelling and Differentiable Simulations. In *International Conference on Learning Representations (ICLR)*, 2023.

- Pathak, P. H., Feng, X., Hu, P., and Mohapatra, P. Visible Light Communication, Networking, and Sensing: A Survey, Potential and Challenges. *IEEE communications surveys & tutorials*, 17(4):2047–2077, 2015.
- Savvides, A., Han, C.-C., and Strivastava, M. B. Dynamic fine-grained localization in Ad-Hoc networks of sensors. In *Proceedings of the 7th ACM Annual International Conference on Mobile Computing and Networking (MobiCom)*, 2001.
- Tancik, M., Casser, V., Yan, X., Pradhan, S., Mildenhall, B., Srinivasan, P. P., Barron, J. T., and Kretschmar, H. Block-NeRF: Scalable Large Scene Neural View Synthesis. In *IEEE/CVF Conference on Computer Vision and Pattern Recognition (CVPR)*, 2022.
- Tian, F., Du, S., and Duan, Y. MonoNeRF: Learning a Generalizable Dynamic Radiance Field from Monocular Videos. In *IEEE/CVF International Conference on Computer Vision (ICCV)*, 2023.
- Tong, S., Wang, J., Yang, J., Liu, Y., and Zhang, J. Citywide LoRa Network Deployment and Operation: Measurements, Analysis, and Implications. In *Proceedings of the 21st ACM Conference on Embedded Networked Sensor Systems (SenSys)*, 2023.
- Trevithick, A. and Yang, B. GRF: Learning a General Radiance Field for 3D Representation and Rendering. In *IEEE/CVF International Conference on Computer Vision (ICCV)*, 2021.
- Van Trees, H. L. *Optimum array processing: Part IV of detection, estimation, and modulation theory*. John Wiley & Sons, 2002.
- Vaswani, A., Shazeer, N., Parmar, N., Uszkoreit, J., Jones, L., Gomez, A. N., Kaiser, Ł., and Polosukhin, I. Attention is all you need. *Advances in Neural Information Processing Systems*, 30:6000–6010, 2017.
- Wang, Q., Wang, Z., Genova, K., Srinivasan, P. P., Zhou, H., Barron, J. T., Martin-Brualla, R., Snavely, N., and Funkhouser, T. IBRNet: Learning Multi-View Image-Based Rendering. In *IEEE/CVF Conference on Computer Vision and Pattern Recognition (CVPR)*, 2021.
- Wang, Z., Bovik, A. C., Sheikh, H. R., and Simoncelli, E. P. Image quality assessment: from error visibility to structural similarity. *IEEE transactions on image processing*, 13(4):600–612, 2004.
- Wong, P.-z., Koplik, J., and Tomanic, J. Conductivity and permeability of rocks. *Physical Review B*, 30(11):6606, 1984.
- Xu, M., Zhan, F., Zhang, J., Yu, Y., Zhang, X., Theobalt, C., Shao, L., and Lu, S. WaveNeRF: Wavelet-based Generalizable Neural Radiance Fields. In *IEEE/CVF International Conference on Computer Vision (ICCV)*, 2023.
- Yang, K., Chen, Y., and Du, W. OrchLoc: In-Orchard Localization via a Single LoRa Gateway and Generative Diffusion Model-based Fingerprinting. In *Proceedings of the 22nd ACM International Conference on Mobile Systems, Applications, and Services (MobiSys)*, 2024.
- Yun, Z. and Iskander, M. F. Ray tracing for radio propagation modeling: Principles and applications. *IEEE Access*, 3:1089–1100, 2015.
- Zhao, J.-S. and Chew, W. C. Integral Equation Solution of Maxwell’s Equations from Zero Frequency to Microwave Frequencies. *IEEE transactions on antennas and propagation*, 48(10):1635–1645, 2000.
- Zhao, X., An, Z., Pan, Q., and Yang, L. NeRF²: Neural Radio-Frequency Radiance Fields. In *Proceedings of the 29th ACM Annual International Conference on Mobile Computing and Networking (MobiCom)*, 2023.

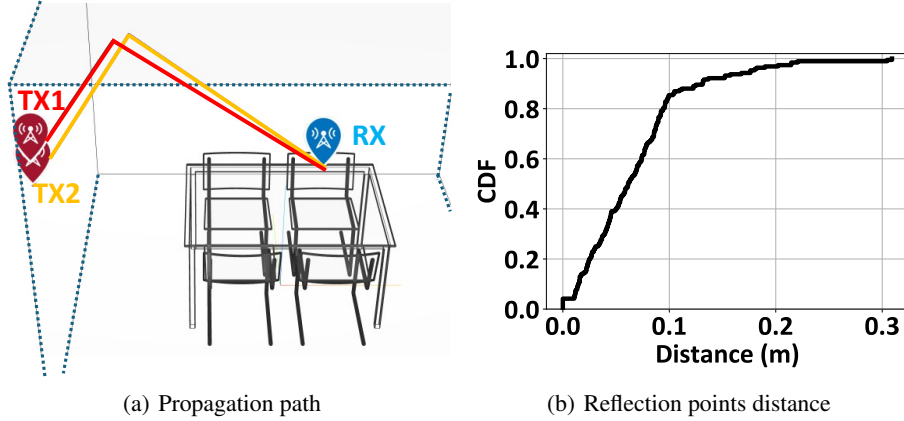


Figure 8. Signal propagation path differences between two transmitters (TXs) and a receiver (RX).

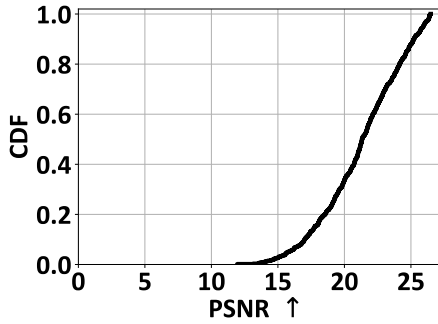


Figure 9. PSNR for using neighbors' spectra.

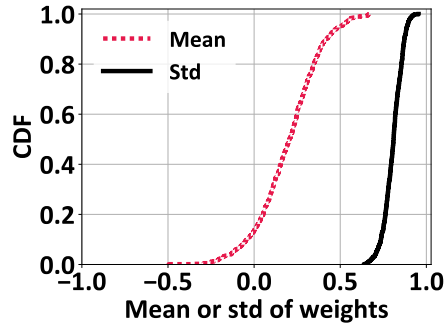


Figure 10. Statistics of the interpolation matrix.

A. Why Incorporate Neighbors

The rationale is based on two observations highlighted in this subsection. First, for a given target transmitter, neighboring transmitters typically traverse similar propagation paths, i.e., they pass through many common voxels within the scene. Second, the spectrum for the target transmitter can be perceived as an interpolation of the spectra from its neighbors. Consequently, leveraging the spectra from these neighbors facilitates the spectrum generation for the target transmitter, thereby improving the generalization ability as long as neighbor data is available. We conduct two empirical experiments to demonstrate these two observations.

Observation #1. In a conference room, as depicted in Figure 8(a), we position the RX at a fixed location and place TX1 and TX2 at two closely situated positions. We utilize the MATLAB ray tracing simulation (MATLAB, 2023) to conduct wireless ray tracing analysis. This software calculates all the propagation paths between the transmitters and the receiver. For brevity, we present one path from either TX1 or TX2 to the RX in Figure 8(a). It is evident that the starting and reflection positions of the two paths are very close, and they both terminate at the RX.

For a more general case, we generate 500 pairs of closely positioned TX1 and TX2, execute the Wireless Insite ray tracing algorithm for each pair, and then compare the distances between the reflection points of their corresponding paths. Figure 8(b) shows that approximately 80% of the distances between reflection points are less than 0.1 m. Given their close starting positions, proximate reflection points, and identical end positions, these factors collectively indicate a similar propagation path. Moreover, assuming the voxel size equals the wavelength, such as 0.13 m for 2.4 GHz WiFi, the path differences are typically less than the voxel size. Therefore, the propagation paths for closely positioned transmitters typically pass through many common voxels.

Observation #2. Given that closely positioned transmitters pass through many common voxels, their spectra may exhibit some correlations. To verify this, we conduct an experiment using RFID dataset (details in Section 5.1). For each transmitter and its corresponding spectrum, we identify the 6 closest positions of other transmitters as its neighbors. We then assign a

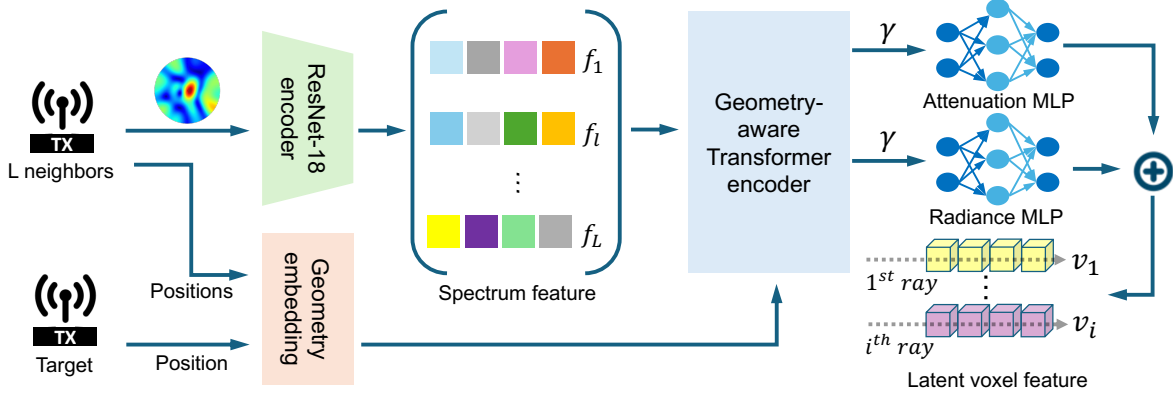


Figure 11. Architecture of geometry-aware wireless scene representation module, consisting of a ResNet feature extractor, geometry embedding, a Transformer encoder, and two MLPs, where a circle with a plus symbol signifies concatenation.

weight matrix to each neighbor; since the spectrum size is $(360, 90)$, each weight matrix is also $(360, 90)$, with every pixel of the spectrum assigned a specific weight. Using each neighbor’s spectrum and its assigned weight matrix, we perform a weighted summation of all neighbors’ spectra to predict the target transmitter’s spectrum. We employ the MSE loss to train the 6 weight matrices over 200 iterations for each target transmitter. Once trained, we compare the generated spatial spectrum with the ground truth spectrum.

Figure 9 illustrates that an average PSNR of 20.5 dB with a standard deviation of 4.1 dB is achieved for the interpolated spatial spectra. To understand what the value of 20.5 dB represents, refer to the second row, first column of Figure 6, which displays a PSNR of 19.5 dB between two spatial spectra. Visually, the similarity between them is apparent. Thus, an average PSNR of 20.5 dB suggests that the neighbors’ spectra are indeed closely related to the target transmitter’s spectrum. Consequently, the target transmitter’s spatial spectrum can be viewed as an interpolation of the spectra of its neighbors. Explaining this phenomenon from a broader perspective, novel view synthesis in the context of visible light can be achieved by interpolating between images captured from different camera poses and views (Chen & Williams, 1993). Similarly, wireless signals may also exhibit such properties. Because visible light and wireless signals are both forms of electromagnetic waves, they might share underlying interpolation characteristics.

You might wonder whether this interpolation method could be directly applied to synthesize spectra for a target transmitter. The answer is NO. First, although the generated spectrum shows promise, it is not sufficiently accurate. Second, the weight matrices are highly dependent on the transmitter positions. A set of weight matrices from one transmitter cannot be applied to another transmitter. We normalize all learned weight matrices for all transmitters and present their mean and standard deviation in Figure 9. It can be observed that the values range from -1.0 to 1.0 , covering all possible values. Thus, the values of the weight matrix are highly dynamic, and a single set of weight matrices cannot be used for other transmitters.

B. Network Architecture

Figure 11 illustrates the architecture of our wireless scene representation module. It comprises a ResNet-18 feature encoder (He et al., 2016), geometry embedding, a geometry-aware Transformer encoder with a cross-attention mechanism (Gheini et al., 2021), and two MLP networks.

To extract compact spectral features from the neighboring spectra, we utilize a ResNet-18 encoder with filter settings of 64, 128, 256, and 512 (He et al., 2016). Both the wireless scene representation and the neural-driven ray tracing algorithm are implemented with a Transformer-based architecture. A typical Transformer consists of multiple stacked blocks; each block contains an attention layer, followed by a residual connection from the input to the post-attention layer, and then layer normalization (LayerNorm). Subsequently, a Feed-Forward Network (FFN) with Rectified Linear Unit (ReLU) activation is applied. This is followed by another residual connection from the output of the first LayerNorm to the output of the ReLU, and the sequence concludes with a second LayerNorm.

The Transformers in both the wireless scene representation and the ray tracing algorithm consist of two stacked blocks, each with a hidden dimension of 16, matching the voxel latent feature dimension d . However, there are two key differences

between these two Transformers. First, the attention mechanisms differ. The scene representation module incorporates a single-headed cross-attention layer, as described in Equation (9), while the ray tracing Transformer uses a multi-headed self-attention layer, as detailed in Equation (11). Second, the handling of token sequential information varies. In the scene representation module, the sequential order of spectrum features is not critical, as the focus lies in the differences between pairs of features. Therefore, the index of the spectrum features is not considered. On the other hand, in the ray tracing algorithm, the sequential information of voxels along a ray is essential, as it directly impacts the calculation of attention weights. Therefore, the index of each voxel along the ray is incorporated.

C. Overhead of *GWRF*.

We report the size and inference time of the model for NeRF and *GWRF* in Table 6. The results indicate that *GWRF* has a larger model size than NeRF, i.e., 27.1 vs. 8.0 MB. Correspondingly, *GWRF* exhibits a longer inference time, i.e., 1.79 vs. 0.43 s. Unlike NeRF, *GWRF* requires neighboring spectra as input. During inference, the target transmitter’s neighbors are extracted from the training dataset, so *GWRF* does not incur additional data burdens. Moreover, since *GWRF* can operate in unseen scenes, it significantly reduces the requirement for a time-consuming training process.

Table 6. Comparison of model size and inference time.

	NeRF ²	<i>GWRF</i>
Model size (MB)	8.0	27.1
Inference time (s)	0.43	1.79